

# The effect of bioturbation and adsorption gradients on solid and dissolved radium profiles in sediments from the eastern equatorial Pacific

DAVID KADKO<sup>1</sup>, J. KIRK COCHRAN<sup>2</sup> and MITCHELL LYLE<sup>1</sup>

<sup>1</sup>College of Oceanography, Oregon State University, Corvallis, OR 97331, U.S.A.

<sup>2</sup>Marine Sciences Research Center, State University of New York, Stony Brook, Long Island, NY 11794, U.S.A.

(Received September 3, 1986; accepted in revised form March 16, 1987)

**Abstract**—Remobilization of Mn resulting from the diagenetic oxidation of organic carbon causes steep adsorption gradients within hemipelagic sediments of the eastern equatorial Pacific. Transport of Ra along these gradients is capable of maintaining marked  $^{226}\text{Ra}$ - $^{230}\text{Th}$  disequilibrium in the surface sediments. Pore water and solid phase  $^{226}\text{Ra}$  profiles measured in cores from two sites in this area are modeled by adjusting the Ra adsorption coefficient as a function of the depth-varying Mn content. At MANOP site M, the high organic carbon accumulation rate causes a sharp redox gradient within the upper 10 cm of sediment. Biological mixing is constant and rapid ( $-500 \text{ cm}^2/\text{kyr}$ ) in this upper layer, below which the Mn content, the Ra adsorption coefficient, and the  $^{226}\text{Ra}/^{230}\text{Th}$  ratio are all sharply reduced. At MANOP site H, the organic carbon accumulation rate is less and therefore the redox gradient is expanded over a greater depth scale. In the surface sediment, biological mixing is slower, decreases with depth, and gradients in the adsorption coefficients and  $^{226}\text{Ra}/^{230}\text{Th}$  ratio are less marked than at site M.

## INTRODUCTION

OXIDATION-REDUCTION REACTIONS associated with early diagenesis of organic matter can strongly influence the chemical nature of the upper abyssal sediment column. During this process, sedimentary organic carbon is oxidized by a characteristic sequence of reactions which proceeds by the reduction of the available oxidant yielding the greatest free energy change per mole of organic carbon oxidized (BENDER *et al.*, 1977; FROELICH *et al.*, 1979; EMERSON *et al.*, 1980; BENDER and HEGGIE, 1984). The sequence in which the oxidants are reduced is everywhere the same:  $\text{O}_2$ ,  $\text{NO}_3^-$ ,  $\text{MnO}_2$ ,  $\text{Fe}_2\text{O}_3$  and  $\text{SO}_4^{2-}$ . In those sediments where carbon accumulates rapidly enough, the reduction of  $\text{MnO}_2$  occurs within centimeters of the sediment-water interface. As the sediment accumulates and is buried beneath the zone of oxygen utilization, manganese is reduced, stripped from the solid phase and mobilized in the porewater. Upward diffusion carries it again to the oxic zone where it is reoxidized and deposited in a discrete, highly enriched layer (FROELICH *et al.*, 1979; KLINKHAMMER, 1980). Such layers have commonly been observed (*e.g.*, LYNN and BONATTI, 1965; LI *et al.*, 1969; GRAYBEAL and HEATH, 1984). The depth of the Mn-rich layer is governed by the balance between  $\text{O}_2$  diffusing downward and  $\text{Mn}^{+2}$  diffusing upward and may be affected by the process of bioturbation (FROELICH *et al.*, 1979; KADKO and HEATH, 1984).

A significant aspect of this process lies in the recognition that manganese oxides are important scavengers of trace metals in the marine environment (JENNE, 1968; MEANS *et al.*, 1978). The unique surface properties of manganese oxides which include a large specific surface area, a high negative surface charge and a high cation adsorption capacity over the pH range of most natural waters (MEANS *et al.*, 1978), enable Mn (IV) minerals to be extremely effective in trace

metal adsorption. Thus, is it likely that the adsorptive characteristics of the upper sediment column can be appreciably altered by the redistribution and concentration of manganese oxide. It has been observed that the distribution of several elements in soils and sediments are markedly influenced by their adsorption onto Mn-oxides. These include Ni, Co, the actinides, Ba and Ra (MEANS *et al.*, 1978; KLINKHAMMER, 1980; KADKO, 1980a; YAMADA and TSUNOGAI, 1981; KADKO and HEATH, 1984; GRAYBEAL and HEATH, 1984; NYFFELER *et al.*, 1984; BALISTRERI and MURRAY, 1986).

The interaction between adsorption and bioturbation can have an appreciable effect upon the transport of material across the sediment-water interface (SCHINK and GUINASSO, 1978; KADKO and HEATH, 1984). Where gradients with depth in the adsorption coefficient exist, the effect of bioturbation will be to increase the volume of sediment effectively exposed to adsorption-desorption reactions with the overlying seawater, and in the process of redistributing particles, to alter the chemical gradients in the interstitial waters associated with these particles. Gradients in adsorption alone can appreciably affect the porewater mobility of dissolved species by altering the effective molecular diffusion coefficient (BERNER, 1976).

In hemipelagic sediments of the eastern equatorial Pacific, conditions are sufficiently reducing that manganese reduction occurs within the top ten or so centimeters, with manganese-enriched layers produced at or near the sediment-water interface. Solid phase  $^{226}\text{Ra}$  profiles measured in the upper sediment column of this area have been modeled by assuming that the adsorption coefficient for radium increases as a function of the solid phase manganese present in the sediment (KADKO, 1980a; KADKO and HEATH, 1984). By applying reasonable values of particle mixing rates, in terms of a biological mixing coefficient  $D_B$  (*e.g.*,

GOLDBERG and KOIDE, 1962), it was found that radium associated with the sediment solids could be reasonably represented by this model. The real test of this representation however, would be if the pore water Ra concentrations could be predicted simultaneously from the model. In this paper we present new solid phase radium and manganese data, as well as two pore water radium profiles, from two sites in the eastern equatorial Pacific. We will show that both the dissolved and solid phase of radium can be reasonably represented by a model in which the radium adsorption coefficient varies as a function of the solid phase manganese content of the sediment. It will be demonstrated that gradients in adsorption resulting from the reduction and reprecipitation of manganese can have a significant influence upon the transport and distribution of reactive species in abyssal sediments.

#### SAMPLE LOCATION AND SITE DESCRIPTION

The cores for this study were taken from two sites (M and H) in the eastern equatorial Pacific (Fig. 1) during the NSF-supported Manganese Nodule Project (MANOP). The overlying waters at the two sites have similar primary productivity, but site M is about 500 m shallower which results in enhanced carbonate preservation, a higher sediment accumulation rate, and over a three-fold higher organic carbon burial rate than at site H (Table 1; MURPHY *et al.*, 1986). The redox gradient at site M is therefore more pronounced, with Mn reduction occurring nearer the sediment-water interface. Manganese oxidation occurs within the upper few centimeters of sediment and solid phase concentrations increase to a maximum (~2%) at the sediment surface. Budgetary considerations indicate that about 80% of the incoming particulate Mn flux is escaping from these sediments into the overlying water (MURPHY *et al.*, 1986). In site H sediments, Mn oxidation and precipitation occur at approximately 10 cm below the sediment-water interface where a peak in solid phase Mn concentration of about 8% is observed. There appears to be no loss of Mn into the

overlying water. Downcore solid phase profiles of Ni and Ra are quite similar to the manganese profiles at these sites (MURPHY *et al.*, 1986; KADKO, 1980a; KADKO and HEATH, 1984) suggesting that both are absorbed onto manganese oxides and released to solution during the reduction of  $Mn^{+4}$  to  $Mn^{+2}$ .

#### SAMPLE ANALYSIS

All cores obtained in this study were taken with the MANOP 2500  $\text{cm}^2$  box corer. Samples from cores IMI7BC13 (site M) and Vulcan-1 BC37 (site H) were obtained by sectioning 6.7 cm plastic piston-subcores of the box cores. Cores Pluto-III MBC15 (site H) and MBC22 (site M) were sampled by sectioning approximately half the box cores over 1–3 cm depth intervals to provide ~1 kg pore water samples. The sampling procedure is similar to that given by COCHRAN and KRISHNASWAMI (1980). Sediment samples were stored refrigerated in sealed polyethylene containers until their return to the laboratory, where the pore water was extracted using a refrigerated centrifuge. Sample sizes ranged from 0.8 to 1.5 kg. All samples were filtered through a 0.45  $\mu\text{m}$  millipore filter using the procedure described in COCHRAN *et al.* (1986). Following filtration, samples were stored acidified until analysis. Pore water  $^{226}\text{Ra}$  analyses were performed by the radon emanation method (MATHIEU, 1977).

Sediment from subcores and the centrifuged large volume samples was dried, powdered and homogenized. Approximately 0.5 g was dissolved in a  $\text{HNO}_3$ ,  $\text{HClO}_4$  and  $\text{HCl}$  solution to which  $^{228}\text{Th}$  and  $^{232}\text{U}$  tracers were added. The solutions were placed in gas washing bottles, purged with He to remove  $^{222}\text{Rn}$ , stored to allow  $^{222}\text{Rn}$  ingrowth, then analyzed for  $^{222}\text{Rn}$  to determine their  $^{226}\text{Ra}$  content. The radon was counted within a zinc sulfide scintillation cell housed against a photomultiplier tube. The sample solution was then passed through a series of cation exchange columns to separate the uranium and thorium isotopes which were finally extracted into TTA and plated onto stainless steel disks. The Th and U isotopes were counted with an alpha spectrometer system consisting of silicon surface barrier detectors and a multi-channel analyzer.

Aliquots of the dried sediment samples were dissolved by a hydrofluoric acid-nitric acid digestion procedure (ROBBINS

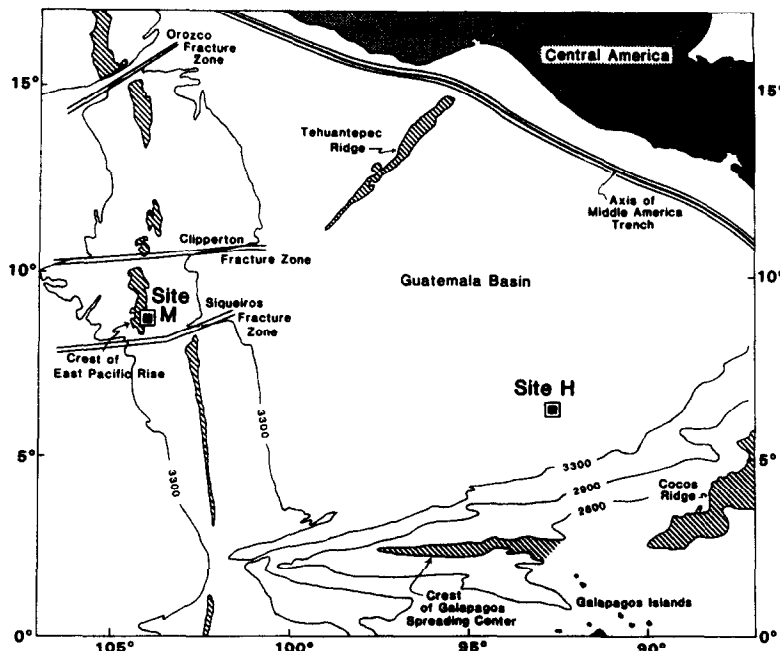


FIG. 1. Location of MANOP sites M and H.

TABLE 1

Comparison of particle and burial fluxes<sup>a</sup> of organic C, CaCO<sub>3</sub> and Mn at sites M and H.

	Site M	Site H
C org	particle flux	138
	burial flux	3.3 ± 0.6
	% preserved	2.4 ± 0.4
CaCO <sub>3</sub>	particle flux	660
	burial flux	37 ± 7
	% preserved	6 ± 1
Mn	particle flux	2.0
	burial flux	0.41 ± 0.08
	% preserved	21 ± 4
Sedimentation rate (cm/kyr)	1.0 <sup>b</sup>	<200 ± 40 0.66 <sup>c</sup>

<sup>a</sup> Fluxes in  $\mu\text{g}/\text{cm}^2/\text{yr}$  (from MURPHY *et al.*, 1986)  
<sup>b</sup> KADKO, 1980a.  
<sup>c</sup> KADKO and HEATH, 1984  
<sup>d</sup> This is a lower limit due to possible particle dissolution in sediment trap cups.

*et al.*, 1984) and analyzed for Mn by atomic adsorption spectrophotometry by the method described in LYLE *et al.*, 1984. The water contents (%H<sub>2</sub>O) were also determined for the Pluto cores by drying aliquots of wet sediment in fixed volume cylinders (18.97 cm<sup>3</sup>), from which salt correction factors, density, and porosity were calculated.

## RESULTS

The pore water <sup>226</sup>Ra data are given in Table 2. Replicate analyses indicate that the precision is  $\sim \pm 10\%$ . Values in core MBC22 (site M) increase from 0.5 dpm/kg near the sediment-water interface to  $\sim 8$  dpm/kg at  $\sim 30$  cm depth. In comparison, core MBC15 (site H) shows relatively little change in pore water <sup>226</sup>Ra with depth, and values are generally less than 1 dpm/kg throughout the core. Because the sediment becomes reducing at depth in each core, oxidation of the sample during storage ( $\sim 30$  days) before separation of the pore water may have affected the pore water <sup>226</sup>Ra concentration. To evaluate this possibility, a few subcores from other box cores taken at site H were sampled for pore water on board the ship to provide composite pore water samples which could be compared with the more detailed data from core MBC15. The pore water was separated in a refrigerated van and sample handling was the same as that for the pore water samples collected for trace metal and nutrient analyses (EMERSON *et al.*, 1980; KLINTHAMMER, 1980). Sample sizes were typically less than 0.1 kg and samples were stored acidified until analysis. The <sup>226</sup>Ra activities of the composite samples ranged from 0.4 to 1.9 dpm/kg with an uncertainty as great as 50% due to small volumes. Values measured in core MBC15 (0.5 to 1.1 dpm/kg) fall within this range and we conclude that, although storage may have affected the pore water <sup>226</sup>Ra activities in core MBC15, the effect is less than a factor of two. This is considerably less than the factor of ten difference in pore water radium between sites H and M which we attribute to differences in the sediment chemistry of the two sites (see below).

The solid phase radiochemical and Mn data are presented in Table 3. The errors indicated are  $1\sigma$  counting

errors for <sup>230</sup>Th and either  $1\sigma$  counting errors or the standard deviation of multiple radon extractions (whichever is greater) for <sup>226</sup>Ra. Some of the data from cores BC13 and BC37 have been presented previously (KADKO, 1980a; KADKO and HEATH, 1984; LYLE *et al.*, 1984). Additional analyses are included here and, unlike some of the earlier tabulations, all the results are presented on a salt-free basis (assuming a pore water salinity of 35‰).

For the site M cores, the maximum Mn concentration (1.5–2%) occurs at the sediment surface and drops off rapidly to 0.1–0.3% below about 10 cm depth. The solid phase <sup>226</sup>Ra concentrations are also high in the surface sediments (39–48 dpm/g) and drop off precipitously below 10 cm depth (13 dpm/g). This trend is the reverse of the pore water <sup>226</sup>Ra profile. The site H solid phase Mn and <sup>226</sup>Ra concentrations, like the pore water <sup>226</sup>Ra profile, show less change with depth than those at site M. A maximum in the solid phase <sup>226</sup>Ra of several dpm/g does, however, coincide with a maximum in the Mn content (7–8%) at approximately 9 cm depth in the site H cores.

The H<sub>2</sub>O contents for cores MBC15 and MBC22 are given in Table 4. The values do not show a large range in either core (72.6%–79.1% for MBC22 and 76.2%–84.0% for MBC15). The porosities were calculated from the formula

$$\phi = \frac{W\rho_s}{W\rho_s + (1 - W)\rho_w} \quad (1)$$

where

$W$  = weight percent H<sub>2</sub>O/100

$\rho_s$  = density of solids (2.7 g/cm<sup>3</sup>)

$\rho_w$  = density of seawater (1.025 g/cm<sup>3</sup>).

The dry bulk density of the sections were measured by

TABLE 2  
<sup>226</sup>Ra activities in sediment pore water

	Depth (cm)	<sup>226</sup> Ra (dpm/kg)*
Site M (Pluto MBC22)		
0 - 2.0		0.46
2.0 - 4.1		1.13
4.1 - 6.1		0.98
6.1 - 8.1		1.60
8.1 - 10.4		2.30
10.4 - 13.2		2.31
13.2 - 16.0	a) 2.36 b) 1.94	
16.0 - 18.7		2.66
18.7 - 21.5	a) 4.69 b) 4.83	
21.5 - 25.1		5.48
25.1 - 28.4		7.05
28.4 - 33.3		7.65
Site H (Pluto MBC15)		
0 - 1.2		1.12
1.2 - 3.6		0.52
3.6 - 6.1		0.51
6.1 - 8.6		0.48
8.6 - 10.9		0.56
10.9 - 12.9		0.73
12.9 - 15.4	a) 0.60 b) 0.63	
15.4 - 18.5		0.60
18.5 - 21.8	a) 0.49 b) 0.40	
21.8 - 26.8		0.55
26.8 - 31.1		0.50
36.3 - 39.3		0.71

\* replicate analyses are denoted by a) and b)

TABLE 3  
Solid Phase Analyses

Depth (cm)	Mn (%)	$^{230}\text{Th}$ (dpm/g)	$^{226}\text{Ra}$ * (dpm/g)
<u>IM17 - BG13 - Site N</u>			
0-1	2.05	32.3 ± 0.5	48.0 ± 1.2
1-2	1.36	30.4 ± 0.3	43.6 ± 1.6
2-3	1.10	31.1 ± 1.0	40.3 ± 1.4
3-4	1.00	-	40.5 ± 1.30
4-5	-	29.3 ± 0.8	45.9 ± 1.55
5-6	0.66	-	47.2 ± 1.3
6-7	-	33.6 ± 0.7	41.8 ± 1.2
7-8	-	-	46.0 ± 0.8
8-9	-	a) 26.8 ± 0.7 b) 26.9 ± 0.7	30.9 ± 0.28 30.2 ± 0.35
9-10	0.28	-	19.2 ± 1.0
10-11	-	-	12.0 ± 0.86
11-12	-	20.1 ± 0.6	-
12-13	-	-	12.7 ± 0.9
13-14	-	25.5 ± 0.2	17.5 ± 0.6
14-15	-	22.5 ± 0.2	16.3 ± 0.7
15-16	-	-	16.2 ± 0.8
16-17	-	-	27.7 ± 1.7
17-18	-	-	-
18-19	-	-	-
19-20	-	-	-
20-21	-	-	-
21-22	-	-	-
22-23	-	-	-
23-24	-	-	-
24-25	-	-	-
25-26	-	-	-
26-27	-	-	-
27-28	-	-	-
28-29	-	-	-
29-30	-	-	-
30-31	-	-	-
31-32	-	-	-
32-33	-	-	-
33-34	-	-	-
34-35	-	-	-
35-36	-	-	-
36-37	-	-	-
37-38	-	-	-
38-39	-	-	-
<u>VULCAN - 37BC - Site N</u>			
0-1	5.35	a) 57.2 ± 1.0 b) 52.2 ± 1.2	- 59.1 ± 2.3
1-2	5.23	46.5 ± 1.1	a) 65.5 ± 3.4 b) 67.3 ± 5.0
2-3	5.19	50.4 ± 0.9	53.0 ± 2.4
3-4	5.27	40.6 ± 0.9	53.2 ± 1.5
4-5	5.60	-	51.8 ± 3.1
5-6	5.96	44.3 ± 0.6	51.2 ± 0.4
6-7	7.12	46.1 ± 0.6	a) 56.8 ± 2.9 b) 59.2 ± 2.4
7-8	-	-	-
8-9	-	-	-
9-10	6.68	37.8 ± 0.5	56.1 ± 2.0
10-11	-	-	49.5 ± 1.0
11-12	3.96	36.2 ± 1.3	-
12-13	-	-	34.3 ± 0.7
13-14	2.34	-	a) 40.8 ± 0.6 b) 42.4 ± 2.8
14-15	-	-	-
15-16	2.21	38.6 ± 0.8	-
16-17	-	-	-
17-18	2.13	-	37.4 ± 0.2
18-19	-	-	-
19-20	2.13	33.5 ± 0.7	-
20-21	-	-	-
21-22	2.20	-	-
22-23	-	-	-
23-24	-	-	-
24-25	-	-	-
25-26	-	-	-
26-27	1.81	34.3 ± 0.5	39.1 ± 2.2
27-28	-	-	-
28-29	1.80	-	35.6 ± 2.7
29-30	-	-	-
30-31	1.66	29.9 ± 0.6	30.5 ± 0.9
31-32	-	-	-
32-33	1.57	-	27.2 ± 0.8
33-34	-	-	-
34-35	-	-	-
35-36	-	-	-
36-37	-	-	-
37-38	-	-	-
38-39	0.90	28.2 ± 0.5	-
<u>PLUTO - MRC22 - Site N</u>			
0-2	1.65	40.5 ± 1.2	39.8 ± 0.6
2-4	1.59	-	43.5 ± 1.1
4-6	1.21	39.1 ± 0.5	45.0 ± 1.4
6-8	1.02	-	39.1 ± 1.7
8-10	0.79	-	a) 40.0 ± 3.8 b) 39.0 ± 1.5
10-12	-	-	-
12-14	-	-	-
14-16	0.37	42.0 ± 0.7	21.5 ± 0.6
16-18	-	-	-
18-20	0.14	a) 24.8 ± 0.4 b) 25.2 ± 0.4	14.3 ± 1.2
20-22	-	-	-
22-24	0.10	-	13.3 ± 0.2
24-26	-	-	13.1 ± 0.5
26-28	0.09	31.3 ± 0.6	15.0 ± 0.7
28-30	-	-	17.7 ± 1.3
30-32	0.10	-	-
32-34	0.11	-	-
34-36	0.12	25.9 ± 0.5	19.0 ± 0.6
<u>PLUTO - MRC15 - Site N</u>			
0-1	4.95	a) 70.0 ± 1.0 b) 63.4 ± 0.7	61.6 ± 0.1 62.7 ± 1.9
1-2	-	-	a) 55.3 ± 1.9 b) 56.7 ± 0.9
2-3	6.29	-	a) 50.7 ± 3.1 b) 44.5 ± 1.6
3-4	-	-	56.5 ± 1.6
4-5	6.15	57.9 ± 1.0	53.0 ± 1.1
5-6	8.07	-	-
6-7	-	-	53.0 ± 1.1
7-8	7.13	44.2 ± 0.8	a) 39.1 ± 1.7 b) 56.5 ± 1.5
8-9	-	-	-
9-10	4.98	a) 47.8 ± 0.7 b) 42.8 ± 0.5	53.7 ± 0.2
10-11	-	-	-
11-12	3.57	44.6 ± 0.9	48.9 ± 1.1
12-13	-	-	-
13-14	2.56	-	39.2 ± 1.6
14-15	-	-	-
15-16	2.33	-	38.1 ± 1.0
16-17	-	-	-
17-18	2.35	43.0 ± 0.6	35.5 ± 1.9
18-19	-	-	-
19-20	1.90	-	31.2 ± 0.2
20-21	3.63	30.9 ± 0.3	28.8 ± 0.1
21-22	1.63	-	-
22-23	-	-	-
23-24	1.28	-	25.0 ± 0.3

\* disintegrations per minute per gram of dry, salt-free sediment.  
Replicate measurements are denoted by a) and b).

dividing the dried sediment weight by the volume of total wet sediment. This compared well to the values obtained by the formula

$$\rho_d = \frac{(1-W)}{W/\rho_w + (1-W)/\rho_s} \quad (2)$$

These results are presented in Table 4.

## DISCUSSION

### I. Radium models

a. *Oxic sediments.* In oxic pelagic sediments, profiles of solid phase and porewater  $^{226}\text{Ra}$  ( $t_{1/2} = 1620$  yrs) appear to conform to a distribution dictated by a balance between molecular diffusion, bioturbation, production from its parent  $^{230}\text{Th}$  ( $t_{1/2} = 75,000$  yrs), radioactive decay, and advection (sedimentation) (COCHRAN and KRISHNASWAMI, 1980; KADKO, 1980b). Typically, the solid phase of radium will be depleted relative to its parent  $^{230}\text{Th}$  in the upper one or two decimeters of sediment, owing to diffusive loss into the overlying water, and to incomplete ingrowth with the thorium. At depth, equilibrium between the two isotopes is approached. The pore water concentrations increase with depth from the bottom water value at the sediment-water interface to a maximum, then decrease owing to the fact that the  $^{226}\text{Ra}$  production rate ( $^{230}\text{Th}$  activity) decreases with depth (Fig. 2).

Reasonable sediment radium profiles have been generated by a model which partitions the radium into three phases: solid, adsorbed and dissolved. In this model, input of particulate  $^{226}\text{Ra}$  from the overlying water is considered insignificant, and the production from excess  $^{230}\text{Th}$  in the sediment is the major source of the radium. The solid (or immobile) phase is described by

$$\frac{\delta \text{Ra}}{\delta t} = \frac{\delta}{\delta z} \left( D_B \frac{\delta \text{Ra}}{\delta z} \right) - S \frac{\delta \text{Ra}}{\delta z} - \lambda \text{Ra} + PF \quad (3)$$

TABLE 4  
Water content, porosity and dry bulk density measurements on Pluto cores

Depth (cm)	$H_2O(\%)^a$	$\phi^b$	calc <sup>c</sup>	meas <sup>d</sup>
<u>MRC22 (Site N)</u>				
0-2	79.1	0.91	0.246	0.266
2-4	76.6	0.89	0.281	0.234
4-6	78.9	0.91	0.249	0.259
6-8	76.8	0.89	0.278	0.281
8-10	73.7	0.88	0.322	0.326
10-12	72.6	0.88	0.338	0.341
12-14	70.9	0.87	0.364	0.336
14-16	77.2	0.90	0.272	0.289
16-18	75.1	0.89	0.302	0.315
18-20	73.3	0.88	0.328	0.324
20-22	73.0	0.88	0.332	0.362
22-24	73.2	0.88	0.329	0.347
24-26	73.5	0.88	0.325	0.323
26-28	75.9	0.89	0.290	0.301
28-30	74.1	0.88	0.316	0.312
<u>MRC15 (Site N)</u>				
0-2	-	-	-	-
2-4	83.0	0.93	0.194	0.187
4-6	82.4	0.92	0.203	0.210
6-8	81.9	0.92	0.209	0.206
8-10	76.8	0.89	0.278	0.283
10-12	84.0	0.93	0.182	0.207
12-14	79.7	0.91	0.238	0.249
14-16	80.0	0.91	0.234	0.241
16-18	78.5	0.91	0.254	0.249
18-20	78.3	0.90	0.257	0.272
20-22	78.1	0.90	0.260	0.276
22-24	78.4	0.90	0.256	0.249
24-26	78.0	0.90	0.261	0.308
26-28	78.2	0.90	0.258	0.254
28-30	78.2	0.90	0.258	0.271
30-32	76.2	0.89	0.286	0.296
32-34	79.0	0.91	0.247	0.244

a. calculated as grams pore water ( $\rho=1.025$ ) per gram wet sediment  $\times 100$

b. porosity calculated from equation 1 in text

c. dry bulk density calculated from equation 2 in text (grams dry, salt-free sediment per cm<sup>3</sup> total sediment volume).

d. dry bulk density calculated by dividing dry, salt-free sediment weight by volume of total wet sediment.

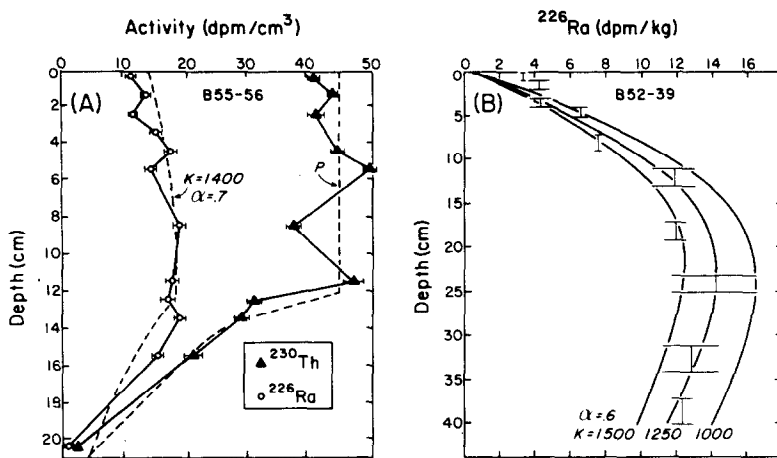


FIG. 2. (A)—Solid phase  $^{226}\text{Ra}$  and  $^{230}\text{Th}$  from core 55-56 from DOMES site B. Also shown are the model-generated profile for  $^{226}\text{Ra}$ , and the  $^{230}\text{Th}$  production rate ( $P$ ) used in the model (KADKO, 1980b). Core location  $11^{\circ}50.3'\text{N}$ ,  $137^{\circ}28.2'\text{W}$ ; water depth 4892 m. (B)—Pore water  $^{226}\text{Ra}$  profile from core 52-39 from DOMES site B. Also shown are model-generated profiles for various values of  $K$  (COCHRAN and KRISHNASWAMI, 1980). Core location  $11^{\circ}14.8'\text{N}$ ,  $139^{\circ}4.1'\text{W}$ ; water depth 4831 m.

where

$\text{Ra}$  = concentration of radium in the solid phase (dpm/cm<sup>3</sup>)

$D_B$  = biological mixing coefficient (cm<sup>2</sup>/kyr)

$S$  = sedimentation rate (cm/kyr)

$P$  =  $^{226}\text{Ra}$  production rate (atoms/cm<sup>3</sup> · kyr), and

$F$  = fraction of radium produced that recoils into the mineral grains and is immobile, that is, not available for pore water-sediment exchange.

For adsorbed radium,

$$\frac{\delta \bar{c}}{\delta t} = \frac{\delta}{\delta z} \left( D_B \frac{\delta \bar{c}}{\delta z} - S \frac{\delta \bar{c}}{\delta z} - \lambda \bar{c} + \frac{\delta \bar{c}}{\delta t} \right)_{\text{eq. ads.}} + P \alpha \quad (4)$$

where

$\bar{c}$  = the concentration of adsorbed  $^{226}\text{Ra}$  (in dpm/cm<sup>3</sup> of total sediment),

$\alpha = (1 - F)$  and is the fraction of radium produced that is available for pore water-sediment exchange,

$\frac{\delta \bar{c}}{\delta t} =$  the change in concentration due to equilibrium adsorption of dissolved  $^{226}\text{Ra}$ .

For dissolved radium,

$$\frac{\delta c}{\delta t} = D_m \frac{\delta^2 c}{\delta z^2} - S \frac{\delta c}{\delta z} - \lambda c + \frac{\delta c}{\delta t} \quad (5)$$

where  $D_m$  is the molecular diffusion coefficient in sediment ( $1.6 \times 10^{-5}$  cm<sup>2</sup>/kyr). Because porosity variations are small over the top 30 cm (Table 4),  $c$ , the concentration of dissolved  $^{226}\text{Ra}$ , also may be expressed in dpm/cm<sup>3</sup> of total sediment. (Note that here the notation for the dissolved and adsorbed concentrations,  $c$  and  $\bar{c}$  respectively, is that used originally in BERNER, 1976, and COCHRAN and KRISHNASWAMI, 1980, and opposite that found in KADKO, 1980a and KADKO and HEATH, 1984.)

In oxic sediments, the manganese content and hence the adsorption properties of the upper 30 centimeters of sediment will be relatively constant. By assuming rapid equilibrium adsorption, the adsorbed and dissolved component may be related by

$$\bar{c} = Kc \quad (6)$$

where  $K$  is the distribution coefficient. In this usage,  $K$  reflects the partitioning of an element between the sediment surfaces and the pore water, and does not refer to a particular reaction mechanism (e.g., BALISTRIERI and MURRAY, 1986). With this relationship, Eqns. (4) and (5) can be coupled and solved analytically by assuming steady state

$$\frac{\delta c}{\delta t} = \frac{\delta \bar{c}}{\delta t} = 0$$

and by use of the following equality:

$$-\frac{\delta c}{\delta t} \Big|_{\text{eq. ads.}} = \frac{\delta \bar{c}}{\delta t} \Big|_{\text{eq. ads.}} \quad (7)$$

The derivation of these relationships are discussed elsewhere in greater detail (COCHRAN and KRISHNASWAMI, 1980; KADKO, 1980b). Figure 2 compares model generated profiles to the radium distribution observed in sediment from DOMES site B in the central Pacific. In these models, biological mixing was fixed at a constant rate in an upper layer of fixed depth, below which no mixing occurred. Values of  $1-5 \times 10^3$  for the adsorption coefficient of radium in pelagic sediments, held constant with depth, have been used in these models. The fraction of radium available for pore water exchange,  $\alpha$ , has been estimated by the  $^{222}\text{Rn}$  emanation characteristics of the sediment (BROECKER, 1965; KEY *et al.*, 1979; COCHRAN and KRISHNASWAMI, 1980; KADKO and HEATH, 1984) and lies in the range of 0.5–0.7 for most oxic, deep sea sediments.

b. Suboxic sediments. In suboxic sediments of the

eastern equatorial Pacific, the concentration-depth profiles of radium are quite different from those found in oxic pelagic sediments. In the upper few centimeters of sediment, within the zone of Mn oxidation, an excess of  $^{226}\text{Ra}$  over  $^{230}\text{Th}$  is often observed (Table 3). Below this, within the zone of Mn-reduction,  $^{226}\text{Ra}$  becomes deficient relative to the  $^{230}\text{Th}$  activity before finally approaching equilibrium at depth (Fig. 3, KADKO, 1980a; KADKO and HEATH, 1984). This distribution is more pronounced at site M, where the redox gradient is sharp, than at site H, where the sequence of reduction reactions is expanded over a greater depth scale.

Radium can be modeled in these sediments using Eqns. (3-7), if  $K$  and  $F$  are allowed to vary with depth as a function of the sedimentary manganese content. To solve these equations, a numerical treatment has been developed which also allows the biological mixing term,  $D_B$ , to be treated as a depth-dependent variable

(Fig. 4, KADKO and HEATH, 1984). In this model, the biological mixing term from Eqn. (3) is expanded:

$$\frac{\delta D_B}{\delta z} \frac{\delta \text{Ra}}{\delta z} + D_B \frac{\delta^2 \text{Ra}}{\delta z^2}. \quad (8)$$

$D_B$  is allowed to vary with depth using the function  $D_B = D_B^0 r^{z-1}$ , where  $D_B^0$  is the mixing coefficient for the sediment surface and  $0 \leq r \leq 1$ . This expression describes the attenuation in bioturbation with depth for  $z \geq 1$ . Numerically, this becomes:

$$\frac{D_B^0}{\Delta z^2} [(r^{z-1} - r^{z-2})(\text{Ra}_z - \text{Ra}_{z-1}) + r^{z-1}(\text{Ra}_{z+1} - 2\text{Ra}_z + \text{Ra}_{z-1}/r)]$$

or

$$\frac{D_B^0}{\Delta z^2} r^{z-1} (\text{Ra}_{z+1} - \text{Ra}_z - \text{Ra}_z/r + \text{Ra}_{z-1}/r). \quad (9)$$

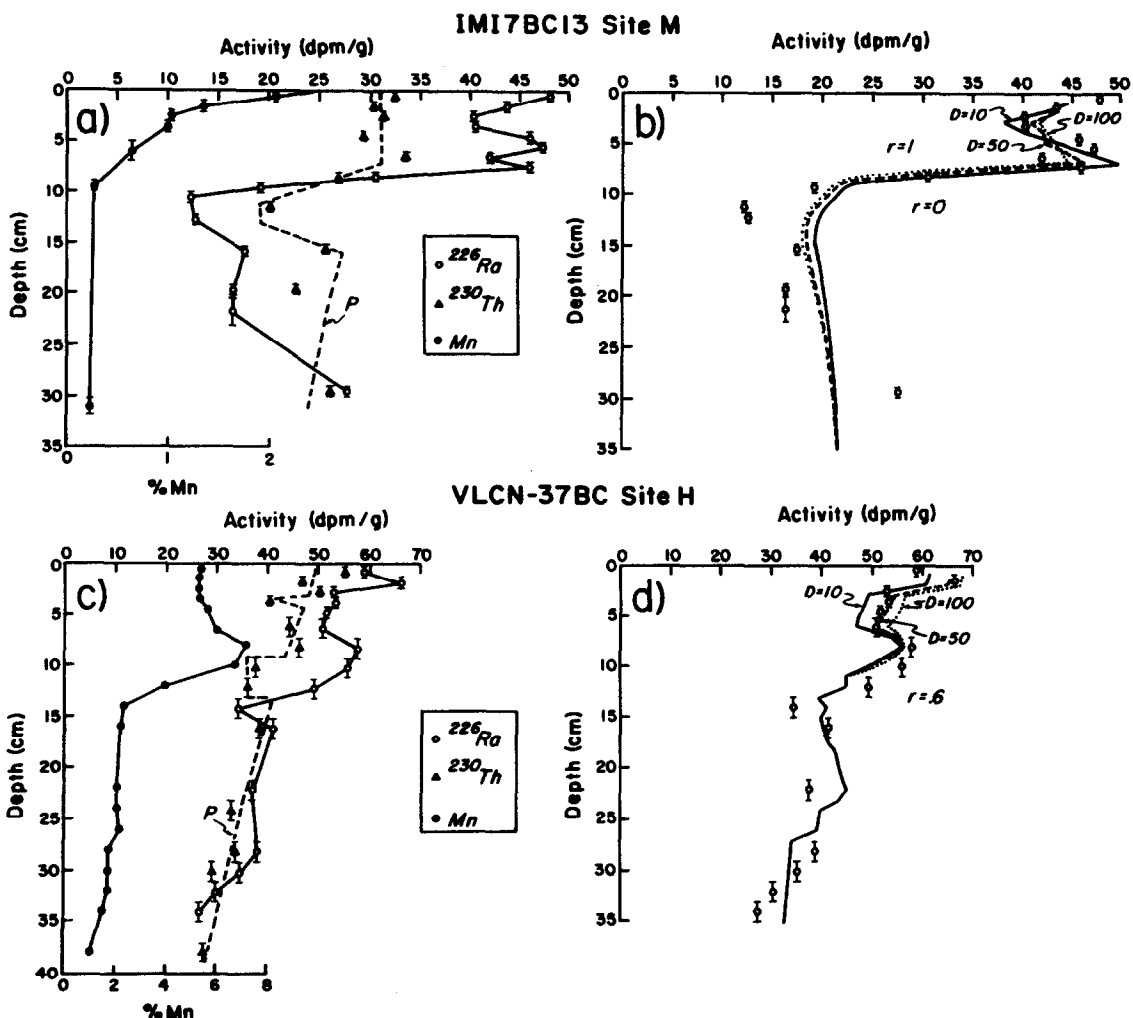


FIG. 3. (A)—Solid phase  $^{226}\text{Ra}$ ,  $^{230}\text{Th}$  and Mn for site M core IMI7BC13. The dashed line indicates the  $^{230}\text{Th}$  production function (P) used in the model (KADKO, 1980a). (B)—Model generated  $^{226}\text{Ra}$  profiles (solid phase) for BC13. Above 8 cm, mixing was constant ( $r = 1$ ) and  $\alpha = .35$ . Below 8 cm, mixing was zero ( $r = 0$ ) and  $\alpha = .90$ . (C)—The solid phase data and (D) the model results for site H core VULCAN 37BC (KADKO and HEATH, 1984). Biological mixing decreased from the surface ( $r = .6$ ). Above 22 cm,  $\alpha = .35$ ; below 22 cm,  $\alpha = .65$ .

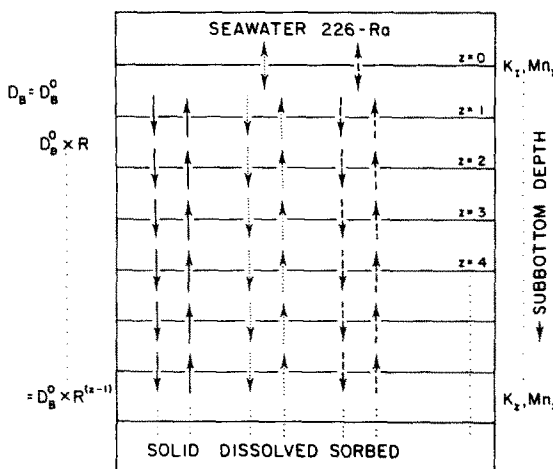


FIG. 4. Schematic diagram of the numerical  $^{226}\text{Ra}$  model. See text for discussion.

$\text{Ra}_z$  is the immobile radium concentration ( $\text{dpm}/\text{cm}^3$ ) in the  $z$ th box. Each box is 1 cm in width, therefore  $\Delta z = \Delta z^2 = 1$ , and these terms are omitted in the following equations.

For the top box ( $0-1$  cm),  $z = 1$ . For  $z < 1$ ,  $r$  and  $\text{Ra}_z$  are defined as zero because respectively, there is no biological mixing above the sediment and we assume that input of particulate  $^{226}\text{Ra}$  from the overlying water is not significant. Equation (3) for  $z = 1$  can then be expressed as:

$$\Delta \text{Ra}_1 = [D_B^0(\text{Ra}_2 - \text{Ra}_1) - S\text{Ra}_1 - \lambda\text{Ra}_1 + PF]\Delta T. \quad (10)$$

For  $z > 1$

$$\begin{aligned} \Delta \text{Ra}_z = & [D_B^0 r^{z-1}(\text{Ra}_{z+1} - \text{Ra}_z - \text{Ra}_z/r \\ & + \text{Ra}_{z-1}/r) - S(\text{Ra}_z - \text{Ra}_{z-1}) - \lambda\text{Ra}_z + PF]\Delta T. \end{aligned} \quad (11)$$

The absorbed radium concentration can be expressed numerically as follows (see Appendix for derivations). For the top box,  $z = 1$ :

$$\begin{aligned} \Delta \bar{\text{c}}_1 = & [D_B^0(\bar{\text{c}}_2 - 2\bar{\text{c}}_1 + K_1 c_{sw}) + D_m \left( \frac{2\bar{\text{c}}_2}{K_2} - \frac{\bar{\text{c}}_1}{K_2} - \frac{\bar{\text{c}}_2}{K_1} + \frac{2\bar{\text{c}}_1}{K_1} \right. \\ & \left. + \frac{\bar{\text{c}}_1}{K_1} + \frac{K_1 c_{sw}}{K_1} \right) - S(\bar{\text{c}}_1 - K_1 c_{sw}) - \lambda\bar{\text{c}}_1 + P\alpha]\Delta T \end{aligned} \quad (12)$$

where  $K_1$  and  $c_{sw}$  are, respectively, the values at the sediment-water interface of the distribution coefficient and the pore water  $^{226}\text{Ra}$  concentration. The value of  $c_{sw}$  is taken to be the concentration of  $^{226}\text{Ra}$  in the overlying seawater, expressed in terms of  $\text{dpm}/\text{cm}^3$  total sediment.

For  $z > 1$

$$\begin{aligned} \Delta \bar{\text{c}}_z = & \left[ D_B^0 r^{(z-1)}(\bar{\text{c}}_{z+1} - \bar{\text{c}}_z - \bar{\text{c}}_z/r + \bar{\text{c}}_{z-1}/r) \right. \\ & + D_m \left( \frac{2\bar{\text{c}}_{z+1}}{K_{z+1}} - \frac{\bar{\text{c}}_z}{K_{z+1}} - \frac{\bar{\text{c}}_{z+1}}{K_z} - \frac{2\bar{\text{c}}_z}{K_z} + \frac{\bar{\text{c}}_z}{K_{z-1}} + \frac{\bar{\text{c}}_{z-1}}{K_z} \right. \\ & \left. \left. - S(\bar{\text{c}}_z - \bar{\text{c}}_{z-1}) - \lambda\bar{\text{c}}_z + P\alpha \right] \Delta T. \right] \quad (13) \end{aligned}$$

The dissolved concentration at any depth, per volume of pore water, will be simply

$$c_z^* = \frac{\bar{c}_z}{K_z \cdot \phi} \quad (14)$$

where  $\phi$  is the sediment porosity. The  $^{230}\text{Th}_{xs}$  production rate used is based on the measured  $^{230}\text{Th}$  profiles. As mentioned previously, the fraction of the production,  $\alpha$ , that is available for pore water-sediment exchange (*i.e.*, the fraction of new  $^{226}\text{Ra}$  recoiled into the pore water) has, for oxic sediments, been estimated from the  $^{222}\text{Rn}$  emanation/total  $^{226}\text{Ra}$  ratio and lies in the range 0.5–0.7. For suboxic sediments, the formation of Mn oxides should affect the fraction of  $^{226}\text{Ra}$  that is recoiled. Manganese oxide coatings formed in the oxic layer may diminish the recoil of  $^{226}\text{Ra}$  into the pore water (lowering  $\alpha$ ), whereas in the reducing zone, the sediments have no such coatings and  $\alpha$  should be larger than in the oxic zone. If in addition, the incorporation of  $^{226}\text{Ra}$  into precipitating authigenic Mn oxyhydroxide phases is important, then changes in concentration due to authigenic mineral formation would be represented by a

$$-\frac{\partial c}{\partial t} \Big|_{\text{auth.}}$$

term in the dissolved phase equation and a

$$+\frac{\partial \text{Ra}}{\partial t} \Big|_{\text{auth.}}$$

term in the solid phase equation. In our model, however, we consider uptake of radium "upon" the forming phases rather than incorporation "into" the phases. We assume furthermore, that the adsorption coefficient,  $K$ , is a linear function of %Mn. Recent laboratory studies on MANOP sediments and sediments from the Panama Basin have indicated that the adsorption coefficient of Ba, which is chemically similar to Ra, is linearly related to the Mn content (BUCHOLTZ, 1986; BALISTRIERI and MURRAY, 1986). To establish this function for our cores, an initial value of  $K_1$  and the corresponding surface %Mn is used with the  $K$  and %Mn values for oxic sediments ( $\sim 10^3$  and .3% respectively) to establish a linear relationship between  $K$  and %Mn. The slope of this function, as well as values of  $\alpha$ , are adjusted until the model profiles best fit the data. The mixing parameters  $D_B^0$  and  $r$  can be constrained by particle mixing rates estimated from  $^{210}\text{Pb}$  profiles. In earlier modeling efforts, the lack of pore water  $^{226}\text{Ra}$  concentrations limited the evaluation of the  $K$ -Mn functionality, although reasonable fits to the solid phase data were obtained (Fig. 3, KADKO, 1980a; KADKO and HEATH, 1984). The pore water concentrations presented here allow us to place firmer constraints on the value of the adsorption coefficients and to test if earlier choices based solely on the solid phase data were reasonable.

The model is run until it reaches steady-state. The

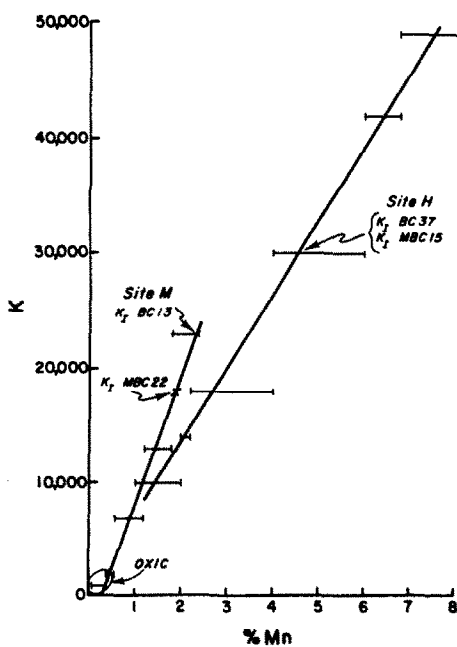


FIG. 5. Model adsorption coefficients ( $K$ ) used for the solid phase radium profiles from cores IMI7-BC13 (site M) and VULCAN 37BC (site H) plotted against Mn content (%). These relationships were then applied to Pluto cores MBC22 and MBC15. The sediment-water interface values ( $K_s$ ) are indicated. Horizontal bars encompass the range of manganese concentration assigned to each discreet value of  $K$  used in the model.

resulting total concentration of  $^{226}\text{Ra}$  per gram of sediment is:

$$^{226}\text{Ra}_z = [\text{Ra}_z + \bar{c}_z + \bar{c}_z/K_z]/\rho_z + U_z \quad (15)$$

where  $\rho$  is the dry bulk density and  $U$  is the background radium contribution from detrital uranium in the sediment (we use 1.2 dpm/g as an average value here). We assume that this constitutes a negligible source of radium for pore water exchange.

## II. Application of the model to MANOP sites M and H

The model results based on solid phase  $^{226}\text{Ra}$  profiles in two cores from sites M and H are shown in Fig. 3 along with the Mn profiles and the  $^{230}\text{Th}$  production function (KADKO, 1980a; KADKO and HEATH, 1984). The  $K$ -Mn functionality used for these models is shown in Fig. 5. Several values of the biological mixing coefficient ( $D_B^0$ ) were tried. For site M, it was found that constant mixing ( $r = 1$ ) confined to the Mn-oxidation zone (0–8 cm) resulted in the best fit to the data. For site H, mixing had to decrease with depth ( $r = 0.6$ ) so that the Mn peak at 8 cm would not be "wiped out." Reasonable fits to the data were generated by this model but two questions arise: 1) Will the adsorption coefficients and other parameters applied to these cores also be suitable for other cores from the same site? 2) Will the pore water profiles generated by the modeled adsorption coefficients (which were based solely on the solid phase distribution) resemble the observed profiles? To answer these questions, we applied the  $K$ -Mn functionality derived from the solid phase modeling to two new cores from these sites on which both solid and dissolved  $^{226}\text{Ra}$  were measured. In Fig. 6a, the  $^{226}\text{Ra}$ ,  $^{230}\text{Th}$  production, and Mn profiles are presented for site M core MBC22. In Figs. 6b and 6c, the model generated profiles are compared to both the measured solid phase and dissolved profiles and it is seen that the trends of the data are followed reasonably well for both phases. Bioturbation rates  $D_B^0 > 100 \text{ cm}^2/\text{kyr}$ , held constant with depth ( $r = 1$ ) in the upper 9 cm, are required to fit the solid phase radium profile and these values are consistent with the mixing rate of  $500 \text{ cm}^2/\text{kyr}$  determined from the excess  $^{210}\text{Pb}$  profile in this core (COCHRAN, 1985). The choice of  $D_B^0$  is much less critical for the dissolved profile. By also allowing  $\alpha$  to be greater in the reduced zone than in the oxic zone ( $\alpha_R > \alpha_O$ ) a better fit to both the pore water and solid

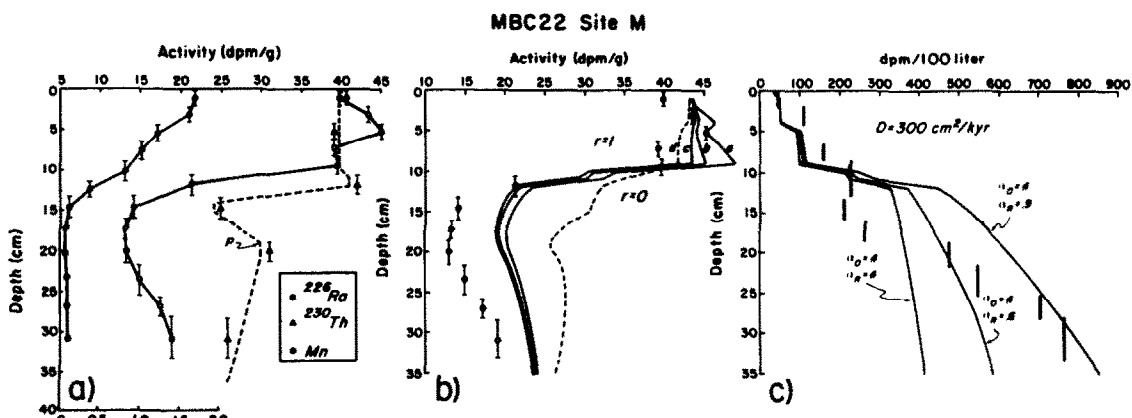


FIG. 6. (A) Solid phase  $^{226}\text{Ra}$ ,  $^{230}\text{Th}$  and Mn from site M core MBC22. The dashed line indicates the  $^{230}\text{Th}_{\text{ox}}$  production function used to model the radium. (B) The model-generated solid phase  $^{226}\text{Ra}$  profile. The solid lines a, b, c are, respectively, the profiles for  $D_B^0 = 100, 300$  and  $600 \text{ cm}^2/\text{kyr}$  with  $\alpha_O = .4$  and  $\alpha_R = .9$ . The dashed line is for the case  $D_B^0 = 300 \text{ cm}^2/\text{kyr}$  with  $\alpha_O = \alpha_R = .4$ . Mixing is constant ( $r = 1$ ) above, and zero ( $r = 0$ ) below, 9 cm and (C) model-generated pore water  $^{226}\text{Ra}$  profiles for site M core MBC22. The solid bars in (C) are the measured pore water concentrations.

phase profiles is obtained. Note that "kinks" in the model-generated profiles are the result of abrupt changes in the values of  $K$  which correspond to rapid changes in the Mn content. The use of boxes smaller than 1 cm width would produce a smoother profile, but since the sampling intervals were greater than 1 cm, finer resolution in the model is not warranted.

In Fig. 7a, the  $^{226}\text{Ra}$ ,  $^{230}\text{Th}$  production and Mn profiles are presented for site H core MBC15. In Figs. 7b and 7c the model generated profiles are again compared to the observed profiles. The solid phase peak in  $^{226}\text{Ra}$  is well defined by the model when  $D_B^0 = 5-50 \text{ cm}^2/\text{kyr}$  and  $r = 0.8$ . The value of  $D_B$  is again in agreement with the  $^{210}\text{Pb}$  mixing rate of  $40 \text{ cm}^2/\text{kyr}$  determined for this core (COCRAN, 1985). For the pore water, the model approximates the observed profile for  $z > 15 \text{ cm}$ , but underestimates the measured concentration in the upper few centimeters. Two possible reasons for this are 1) the high measured surface concentrations are an artifact of sampling. 2) There exists another source of radium that has not been accounted for in the model, such as the reduction of a labile phase near the sediment-water interface (KALHORN and EMERSON, 1984), or the dissolution of Mn-rich particles that have been transported from the continental margins (LI, 1981). The high pore water  $^{226}\text{Ra}$  concentrations measured near the sediment surface, particularly that of the 0–1.2 cm interval, cannot be derived from the model because the surface boundary condition requires only that equilibrium be maintained between the seawater and surface pore water concentrations.

The  $^{226}\text{Ra}$  profiles at sites M and H can be interpreted in terms of several important differences between the sites. The modeled and observed pore water  $^{226}\text{Ra}$  concentration at the base of the box core at site M ( $\sim 7.5 \text{ dpm/l}$ ) is about an order of magnitude greater than that of site H ( $0.7 \text{ dpm/l}$ ). This corresponds to the order of magnitude difference in the burial concentration of Mn between the two sites (0.1–0.3% at M and  $\sim 1\%$

at H) which results in a smaller radium adsorption coefficient at depth for M ( $K \sim 1000$ ) than at H ( $K = 10,000$ ). These differences can be attributed to the greater  $C_{\text{org}}$  burial rate at site M which produces a sharper redox gradient within the sediment column.

Furthermore, it has been recognized that the difference in redox conditions between sites M and H affects the flux of Mn across the sediment-water interface (MURPHY *et al.*, 1986). At M, where Mn-reduction is relatively close to the sediment surface, approximately 80% of the particulate Mn input is lost back into the overlying water. At H, input of particulate Mn is either less than or, if possible dissolution of sediment trap particles is taken into account, matches the burial rate (Table 1; MURPHY *et al.*, 1986). The behavior of  $^{226}\text{Ra}$  is similar to that of Mn at these sites. At M, there is a net flux of  $^{226}\text{Ra}$  out of the sediments. At H, the higher interfacial Mn concentration and thicker oxic zone act not only to cap the sediment with respect to  $^{226}\text{Ra}$ , but coupled with bioturbation the adsorption gradient at the interface drives a net inward flux. An additional source of  $^{226}\text{Ra}$ , if any, could be the same as that postulated for Mn, which involves the dissolution or reduction of Mn-rich phases at the sediment-water interface (LI, 1981; KALHORN and EMERSON, 1984). In Table 5, the modeled flux as a function of bioturbation is listed for the cores from sites M and H. The flux is given by

$$J = \frac{D_B^0}{\Delta z} (c_{\text{sw}} \cdot K_1 - \bar{c}_1) + \frac{D_m}{\Delta z} \left[ c_{\text{sw}} \cdot K_1 \left( \frac{1}{K_1} - \frac{1}{K_2} \right) + \frac{1}{K_1} (c_{\text{sw}} \cdot K_1 - \bar{c}_1) \right] + S \cdot c_{\text{sw}} \cdot K. \quad (16)$$

The effect of bioturbation is to increase the net flux in either direction.

The results of this study suggest that the rate of biological mixing is greater at site M than at site H. A more active benthic community at site M may be sus-

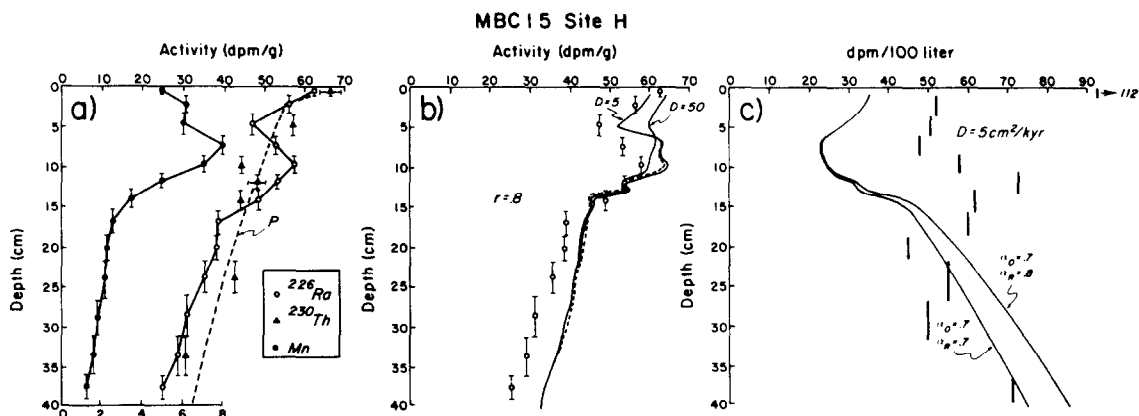


FIG. 7. (A) Solid phase  $^{226}\text{Ra}$ ,  $^{230}\text{Th}$  and Mn from site H core MBC15. The dashed line indicates the  $^{230}\text{Th}_{\text{xs}}$  production function used to model the radium. (B) The model generated solid phase  $^{226}\text{Ra}$  profile. The solid lines are the profiles for  $\alpha_O = \alpha_R = .7$ . The dashed line is the profile for  $D_B^0 = 5 \text{ cm}^2/\text{kyr}$  with  $\alpha_O = .7$  and  $\alpha_R = .8$  and (C) pore water  $^{226}\text{Ra}$  profiles for site H core MBC15. The solid bars in (C) are the measured pore water concentrations.

TABLE 5  
 $^{226}\text{Ra}$  flux at the sediment-water interface  
 at MANOP sites M and H

SITE M		SITE H	
Pluto - MNC22		Pluto - MNC15	
$D_B^0$ (cm <sup>2</sup> /kyr)	Flux*	$D_B^0$ (cm <sup>2</sup> /kyr)	Flux*
100	-60.8	10	+25.3
300	-77.1	50	+28.2
600	-83.3	100	+29.9
<b>IMI7 - BC13</b>		<b>VLGN - BC27</b>	
10	-25.1	10	+38.8
50	-34.9	50	+49.8
100	-39.2	100	+55.4

\* negative values indicate loss of Ra from cores,  
 positive indicates gain of Ra. These values are  
 calculated from equation 16 in text.

tained by the higher organic carbon flux to this site and by the higher organic content of the sediments (1.3% at M and 0.8% at H; MURPHY *et al.*, 1986). This is quite consistent generally with particle mixing rates derived from  $^{210}\text{Pb}$  profiles measured at these sites (COCHRAN, 1985), and specifically, the rates based on  $^{210}\text{Pb}$  for the cores discussed here are quite comparable to those applied to the Ra model. These results are also consistent with the  $^{230}\text{Th}$  distributions in the cores. At site M, the  $^{230}\text{Th}$  content is fairly homogeneous in the mixed zone, while at site H, a gradient is detected in the upper few centimeters which suggests a much slower rate of mixing. It is interesting to note that especially at site M,  $^{230}\text{Th}$  shows a minimum which could be due to remobilization (though to a much lesser extent than radium) immediately below the oxidized zone. This is surprising in light of the generally accepted notion that thorium is essentially immobile in marine sediments, although the possibility of diagenetic mobilization of  $^{230}\text{Th}$  has been discussed by COCHRAN and KRISHNASWAMI, (1980). The data suggest that, although the adsorption coefficient of thorium is much greater than that of radium, a strong gradient in this parameter might be capable of driving some transport through the sediment. The obvious gradient of  $^{230}\text{Th}$  below the oxidized zone at site M also suggests that biological mixing drops off rapidly at that depth, again consistent with the results of radium modeling.

## SUMMARY

Remobilization of manganese which occurs during the diagenetic oxidation of organic carbon can cause steep adsorption gradients within the sediment. Radium-226 profiles measured in cores from two sites in the eastern equatorial Pacific can be modeled by adjusting the adsorption coefficient as a function of the depth-varying manganese content. At MANOP site M, the high organic carbon accumulation rate is responsible for a steep redox gradient which results in rapid changes in adsorption over the upper few centimeters of sediment. Transport of radium along this gradient maintains marked  $^{226}\text{Ra}/^{230}\text{Th}$  disequilibrium in the sediments of this area. To a lesser extent, the sharp

gradient in adsorption may also drive remobilization of thorium. At site M high biological mixing rates which are constant with depth, as evidenced by  $^{230}\text{Th}$  and  $^{210}\text{Pb}$  distributions, are consistent with the  $^{226}\text{Ra}$  modeling results and may be a consequence of the high organic carbon content of the sediments. Below the oxic zone, sharply lower  $^{226}\text{Ra}/^{230}\text{Th}$  activity ratios correspond to the reduction of manganese. At site H, the organic carbon accumulation rate is lower and the redox gradient is expanded over a greater depth scale. Biological mixing is slower at the sediment surface and model results require it to decrease with depth. Gradients in adsorption and  $^{226}\text{Ra}/^{230}\text{Th}$  are less extreme than at site M.

**Acknowledgements**—This work was supported by National Science Foundation Grant OCE-8415723 to David Kadko and OCE-8400072 and OCE-8215747 to J. Kirk Cochran. We are grateful to Jennifer Hess and Chi-An Huh for shipboard sampling assistance and to Richard Kovar, Anne Carey and David Schneider for laboratory assistance. Drs. B. Boudreau, J. Thomson and J. L. Reys kindly reviewed the manuscript and offered many helpful suggestions. This is contribution No. 546 from the Marine Science Research Center.

**Editorial handling:** S. E. Calvert

## REFERENCES

- BALISTRERI L. S. and MURRAY J. W. (1986) The surface chemistry of sediments from the Panama Basin: The influence of Mn oxides on metal adsorption. *Geochim. Cosmochim. Acta* **50**, 2235-2243.
- BENDER M. L. and HEGGIE D. T. (1984) Fate of organic carbon reaching the deep sea floor: a status report. *Geochim. Cosmochim. Acta* **48**, 977-986.
- BENDER M. L., FANNING K. A., FROELICH P. N., HEATH G. R. and MAYNARD D. V. (1977) Interstitial nitrate profiles and oxidation of sedimentary organic matter in the eastern equatorial Atlantic. *Science* **198**, 605-609.
- BERNER R. A. (1976) Inclusion of adsorption in the modeling of early diagenesis. *Earth Planet. Sci. Lett.* **29**, 333-340.
- BROECKER W. S. (1965) The application of natural radon to problems in ocean circulation. Symposium on diffusion in ocean and fresh water, (ed.) T. ICHIYE, Lamont-Doherty Geological Observatory, Palisades, N.Y., pp. 116-145.
- BUCHHOLTZ M. R. (1986) Radioisotope mobility across the sediment-water interface in the deep sea. Ph.D. thesis, Columbia University.
- COCHRAN J. K. (1985) Particle mixing rates in sediments of the eastern equatorial Pacific: evidence from  $^{210}\text{Pb}$ ,  $^{239,240}\text{Pu}$  and  $^{137}\text{Cs}$  distributions at MANOP sites. *Geochim. Cosmochim. Acta* **49**, 1195-1210.
- COCHRAN J. K. and KRISHNASWAMI S. (1980) Radium, thorium, uranium and  $^{210}\text{Pb}$  in deep sea-sediments and sediment pore waters from the north equatorial Pacific. *Amer. J. Sci.* **280**, 849-889.
- COCHRAN J. K., CAREY A. E., SHOLKOVITZ E. R. and SURPRENANT L. D. (1986) The geochemistry of uranium and thorium in coastal marine sediments and sediment pore waters. *Geochim. Cosmochim. Acta* **50**, 663-680.
- EMERSON S., JAHNKE R., BENDER M. L., FROELICH P., KLINKHAMMER G., BOWSER C. and SETLOCK G. (1980) Early diagenesis in sediments from the eastern equatorial Pacific: I. Pore water nutrient and carbonate results. *Earth Planet. Sci. Lett.* **49**, 57-80.
- FROELICH P. N., KLICKHAMMER G. P., BENDER M. L., LUEDTKE N. A., HEATH G. R., CULLEN D., DAUPHIN P., HAMMOND D., HARTMAN B. and MAYNARD V. (1979) Early oxidation of organic matter in pelagic sediments of

- the eastern equatorial Atlantic: suboxic diagenesis. *Geochim. Cosmochim. Acta* **43**, 1075–1090.
- GOLDBERG E. D. and KOIDE M. (1962) Geochronological studies of deep-sea sediments by the ionium/thorium method. *Geochim. Cosmochim. Acta* **26**, 417–450.
- GRAYBEAL A. L. and HEATH G. R. (1984) Remobilization of transition metals in surficial pelagic sediments from the eastern Pacific. *Geochim. Cosmochim. Acta* **48**, 965–975.
- JENNE E. A. (1968) Controls of Mn, Fe, Co, Ni, Cu and Zn concentrations in soils and water: the significant role of hydrous Mn and Fe oxides. *Adv. Chem. Ser.* **73**, 337–381.
- KADKO D. (1980a) A detailed study of some uranium-series nuclides at an abyssal hill area near the East Pacific Rise at 8°45'N. *Earth Planet. Sci. Lett.* **51**, 115–131.
- KADKO D. (1980b)  $^{230}\text{Th}$ ,  $^{226}\text{Ra}$  and  $^{222}\text{Rn}$  in abyssal sediments. *Earth Planet. Sci. Lett.* **49**, 360–380.
- KADKO D. and HEATH G. R. (1984) Models of depth-dependent bioturbation at MANOP site H and the Eastern Equatorial Pacific. *J. Geophys. Res.* **89**, 6567–6574.
- KALHORN S. and EMERSON S. (1984) The oxidation state of manganese in surface sediments of the deep sea. *Geochim. Cosmochim. Acta* **48**, 897–902.
- KEY R. M., GUINASSO N. L. and SCHINK D. R. (1979) Emanation of radon-222 from marine sediments. *Mar. Chem.* **7**, 221–250.
- KLINKHAMMER G. (1980) Early diagenesis in sediments from the eastern equatorial Pacific: II. Pore water metal results. *Earth Planet. Sci. Lett.* **49**, 81–101.
- LI Y. (1981) Geochemical cycles of elements and human perturbation. *Geochim. Cosmochim. Acta* **45**, 2073–2084.
- LI Y., BISHOFF J. and MATHIEU G. (1969) The migration of Mn in the Arctic Basin Sediment. *Earth Planet. Sci. Lett.* **7**, 265–270.
- LYLE M., HEATH G. R., and ROBBINS J. M. (1984) Transport and release of transition elements during early diagenesis: Sequential masking of sediments from MANOP sites M and H. Part I. pH5 arctic acid leach. *Geochim. Cosmochim. Acta* **48**, 1705–1715.
- LYNN D. C. and BONATTI E. (1965) Mobility of manganese in deep sea sediments. *Mar. Geol.* **3**, 457–474.
- MATHIEU G. (1977)  $^{222}\text{Rn}$ - $^{226}\text{Ra}$  technique of analysis. In *Annual Report to the Energy Research and Development Administration*. Contract EY 76-S-02-2185, Appendix 1:1–30.
- MEANS J. L., CRERAR D. A., BORCSIK M. P. and DUGUID M. P. (1978) Radionuclide adsorption by manganese oxides and implications for radioactive waste disposal. *Nature* **274**, 44–47.
- MURPHY K. M., DYMOND J., LYLE M., KADKO D. and FINNEY B. F. (1986) Transition metal geochemistry at two sites in the eastern tropical Pacific: control of ferromanganese nodule genesis by organic carbon accumulation. *Earth Planet. Sci. Lett.* (submitted).
- NYFFELER U. P., LI Y. H. and SANTCHI P. H. (1984) A kinetic approach to describe trace-elements distributions between particles and solution in natural aquatic system. *Geochim. Cosmochim. Acta* **48**, 1513–1522.
- ROBBINS J., HEATH G. R. and LYLE M. W. (1984) A sequential extraction procedure for partitioning elements among co-existing phases in marine sediments. Corvallis, Oregon State University, College of Oceanography, Ref. 84-3, 55 p.
- SCHINK D. R. and GUINASSO N. L. (1978) Redistribution of dissolved and adsorbed materials in abyssal marine sediments undergoing biological stirring. *Amer. J. Sci.* **278**, 682–702.
- YAMADA M. and TSUNOGAI S. (1981) Behavior of radium in deep-sea sediments. *Chi Kyū Kagaku* **15**, 53–59.

## APPENDIX

Numerical evaluation of the dissolved and adsorbed radium concentrations. For the dissolved and adsorbed phases, Eqns. (4–7) are combined in terms of the adsorbed concentration,  $\bar{c}$ :

$$\frac{\delta \bar{c}}{\delta t} + \frac{\delta \left( \frac{\bar{c}}{K} \right)}{\delta t} = \frac{\delta}{\delta z} \left( D_B \frac{\delta \bar{c}}{\delta z} \right) + D_m \frac{\delta^2 \left( \frac{\bar{c}}{K} \right)}{\delta z^2} - S \left( \frac{\delta \bar{c}}{\delta z} + \frac{\delta \left( \frac{\bar{c}}{K} \right)}{\delta z} \right) - \lambda \bar{c} \left( 1 + \frac{1}{K} \right) + P_\alpha. \quad (\text{a1})$$

Noting that  $\delta K / \delta t = 0$  and that  $K \gg 1$ , this can be expressed more simply as:

$$\frac{\delta \bar{c}}{\delta t} = \frac{\delta}{\delta z} \left( D_B \frac{\delta \bar{c}}{\delta z} \right) + D_m \frac{\delta^2 \left( \frac{\bar{c}}{K} \right)}{\delta z^2} - S \frac{\delta \bar{c}}{\delta z} - \lambda \bar{c} + P_\alpha. \quad (\text{a2})$$

The dissolved concentration at any depth, per volume of sediment, will be simply

$$c_z = \frac{\bar{c}_z}{K_z}. \quad (\text{a3})$$

Equation (a2) can be expressed numerically by expanding the biological mixing term as before Eqn. (8) and by expanding the molecular diffusion term as follows:

$$D_m \frac{\delta^2 \left( \frac{\bar{c}}{K} \right)}{\delta z^2} = D_m \left[ 2 \frac{\delta \bar{c}}{\delta z} \cdot \frac{\delta \left( \frac{1}{K} \right)}{\delta z} + \bar{c} \frac{\delta^2 \left( \frac{1}{K} \right)}{\delta z^2} + \frac{1}{K} \frac{\delta^2 \bar{c}}{\delta z^2} \right] \quad (\text{a4})$$

numerically, this becomes

$$D_m \left[ \frac{2\bar{c}_{z+1}}{K_{z+1}} - \frac{\bar{c}_z}{K_z} - \frac{\bar{c}_{z+1}}{K_z} - \frac{2\bar{c}_z}{K_z} + \frac{\bar{c}_z}{K_{z-1}} + \frac{\bar{c}_{z-1}}{K_z} \right]. \quad (\text{a5})$$

Equation (a2) can then be transformed to Eqns. (12) and (13) as presented in the text. For stability, note that this treatment requires the products  $D_B \Delta T$  and  $\frac{D_m}{K} \Delta T$  be less than 0.5 at all times.